

MTGS: Multi-Traversal Gaussian Splatting

Tianyu Li^{1,2*} Yihang Qiu^{2*} Zhenhua Wu^{1*}
Carl Lindström⁴ Peng Su² Matthias Nießner³ Hongyang Li²

¹Shanghai Innovation Institute ²OpenDriveLab and MMLab, The University of Hong Kong
³Technical University of Munich ⁴Chalmers University of Technology



Figure 1. **Multi-Traversal Gaussian Splatting (MTGS)** could reconstruct high-fidelity driving scenes from multi-traversal data. *All images are rendered from a MTGS model of the same road block.* (a) This approach preferably handles variations in lighting and shadows, rendering views conditioned on the traversal index (Trv #). (b) The extrapolation quality of MTGS is showcased. It maintains high visual quality, even with lateral shifts of 8 meters (*i.e.*, two lanes). For clarity, we mark a fixed reference point across traversals with a red pin.

Abstract

Multi-traversal data, commonly collected through daily commutes or by self-driving fleets, provides multiple viewpoints for scene reconstruction within a road block. This data offers significant potential for high-quality novel view synthesis, which is crucial for applications such as autonomous vehicle simulators. However, inherent challenges in multi-traversal data often result in suboptimal reconstruction quality, including variations in appearance and

the presence of dynamic objects. To address these issues, we propose Multi-Traversal Gaussian Splatting (MTGS), a novel approach that reconstructs high-quality driving scenes from arbitrarily collected multi-traversal data by modeling a shared static geometry while separately handling dynamic elements and appearance variations. Our method employs a multi-traversal dynamic scene graph with a shared static node and traversal-specific dynamic nodes, complemented by color correction nodes with learnable spherical harmonics coefficient residuals. This approach enables high-fidelity novel view synthesis and provides flexibility to navigate any viewpoint. We conduct extensive experiments on a large-scale driving dataset, nu-

*Equal contribution.

Primary contact: tianyu@opendrive.com

Plan, with multi-traversal data. Our results demonstrate that MTGS improves LPIPS by 23.5% and geometry accuracy by 46.3% compared to single-traversal baselines. The code and data would be available to the public.

1. Introduction

Building photorealistic simulators is crucial for developing safe and robust autonomous vehicles (AVs), which could be adopted to create digital twins for testing autonomous systems [8, 24, 52], or generate diverse data for training end-to-end planning algorithms [2, 9, 12]. To achieve this goal, the fundamental requirement is to synthesize high-fidelity renderings from arbitrary viewpoints while accurately preserving dynamic elements of the driving environment.

Scene reconstruction from recorded sensor data of AVs has gained popularity in recent years for this purpose [3, 35, 45, 47]. However, methods that rely on single traversal logs often suffer from poor view extrapolation quality [10, 14]. In contrast, multi-traversal data covers a wide range of views. Intuitively, reconstruction using multi-traversal data improves quality for viewpoints that deviate from the original sequence. This is because views distributed across multiple lanes provide richer geometric constraints, potentially enabling view interpolation across the entire drivable area.

Nonetheless, reconstructing a high-fidelity scene across multi-traversals is non-trivial. One characteristic of multi-traversal data is that it represents the same shared space, but the collection could span over a large time period. This indicates that effective interpolation across traversals applies to the spatial aspects of the scene only, corresponding to static 3D geometry, while temporal variations, such as scene dynamics and appearance, remain challenging to interpolate. In particular, the sunlight and weather can be mixed, resulting in different exposure, tone, white balance, and shadow. Furthermore, scene dynamics include both moving and parked vehicles, which are also time-variant. As a consequence, naive reconstruction approaches often struggle to model these inconsistencies, leading to blurred outputs or severe artifacts [10, 30].

To this end, we propose Multi-Traversal Gaussian Splatting (MTGS), the first approach able to reconstruct multi-traversal dynamic scenes and thus synthesize photorealistic extrapolated views, as depicted in Fig. 1. Our approach leverages images from multi-traversal sequences to reconstruct a shared static geometry while separately modeling scene dynamics and appearance variations across different traversals. Specifically, we propose a multi-traversal scene graph that builds a shared static node, and dynamic nodes within sub-graphs corresponding to each traversal. This design enables dynamic objects across traversals to be modeled in parallel. In addition, a LiDAR-guided exposure alignment module is introduced to ensure consistent appear-

ance within individual traversal images. We further integrate an appearance node into each traversal subgraph to capture appearance variations in the form of the residual spherical harmonics coefficient. Finally, multiple regularization losses are developed to enhance the geometric alignment between traversals.

To measure the view extrapolation performance of MTGS with prior works fairly, a dedicated benchmark on the public driving dataset, nuPlan [16], is constructed. We select road blocks with multi-traversal data distributed across multiple lanes and evaluate one isolated traversal with minimal spatial overlap with others. Compared to single-traversal reconstruction, our multi-traversal approach consistently improves performance as additional traversals are incorporated, achieving up to an 18.5% improvement on the pixel-level metric (SSIM), 23.5% on the feature-level metric (LPIPS), and 46.3% on the geometry-level metric (absolute depth relative error). Our method also outperforms state-of-the-art approaches across all evaluation metrics.

The contributions are summarized as follows:

- We propose MTGS with a novel multi-traversal scene graph, including a shared static node that represents background geometry, an appearance node to model various appearances, and a transient node to preserve dynamic information.
- MTGS enables high-fidelity reconstruction with extraordinary view extrapolation quality. We demonstrate that the MTGS achieves state-of-the-art performance in driving scene extrapolated view synthesis. It outperforms previous SOTA by 17.6% on SSIM, 42.4% on LPIPS and 35% on AbsRel.

2. Related Work

Driving Scene Reconstruction. Recent approaches on driving scene reconstruction can be categorized into two paradigms: neural radiance fields (NeRF) [27] and 3D Gaussian splatting (3DGS) [17] based methods. NeRF-based methods [35, 39, 47] have shown remarkable success in reconstructing static backgrounds and dynamic agents via neural feature grids. Recent advancements in 3DGS provide a more efficient solution. DrivingGaussian [54], HUGS [53], and Street Gaussians [45] initialize dynamic objects using 3D bounding boxes and utilize the scene graph design that separates static backgrounds and dynamic objects to reconstruct driving scenes. Building upon this foundation, OmniRe [3] models cyclists and pedestrians using Deformable Gaussian [15] nodes and SMPL [25] nodes. SplatAD [11] explores LiDAR rasterization and solves the rolling shutter effect on both image and LiDAR to achieve better results. Yet, existing methods focus on the single traversal setting mainly, *i.e.*, training and evaluating the original video sequence in a view interpolation manner.

This work extends the dynamic scene graph design to a multi-traversal setting and evaluates an extrapolated view of unseen traversal.

Novel View Synthesis in Autonomous Driving. It emphasizes the extrapolation ability in reconstruction models. This topic follows two technical paradigms primarily: regularization-guided and generative-prior-guided. Among regularization-based methods, AutoSplat [18] introduces planar assumptions on the geometry of the road and sky while exploiting the symmetry of foreground objects to reconstruct unseen parts. Vid2Sim [41] enforces patch-normalized depth consistency and adjacent pixel normal vector alignment. Recent research [14, 46, 49] generates novel views with diffusion models conditioned on different features, *e.g.*, images, depth, or LiDAR, to supplement training 3DGS. FreeSim [7] extends the coverage limit of LiDAR and adopts a hybrid generative reconstruction method to add generated views to the reconstruction process progressively. StreetUnveiler [43] removes parking cars, reconstructs occluded background with an inpainting diffusion model, and designs a near-to-far sampling strategy to improve temporal consistency. While these methods achieve photorealistic synthesis, they exhibit prohibitive computational costs and are limited by the quality of generation models. They also fall short of flexibility when inpainting unseen or occluded parts. Our work addresses these gaps through multi-traversal images collected from the real world, and utilizes regularization to achieve better geometry consistency.

Appearance Modeling. It has been a long-standing challenge in neural scene reconstruction. NeRF in the wild [26] pioneered appearance modeling for unstructured photo collections by presenting learnable per-image appearance embeddings. Block-NeRF [33] utilizes camera exposure parameters to optimize per-image appearance embeddings, enabling city-scale reconstruction. Recent works [21, 42, 50] in 3DGS explore appearance modeling similarly. For instance, Kulhanek et al. [19] propose to combine per-Gaussian and per-image appearance embeddings to model appearance variation. These methods aim to solve per-camera appearance alignment with large overlapped regions, or with additional information input. However, they often treat the transient as a distraction and use a semantic mask or uncertainty optimization to remove dynamic objects from the scene. We address the challenge of appearance modeling in multi-traversal AV sensor datasets, characterized by unbounded, non-object-centric, and dynamic scenes. Our approach leverages the inherent appearance consistency within individual traversals and the variations observed across multi-traversals to achieve improved appearance modeling. Moreover, we retain dynamic information to facilitate downstream applications.

Multi-traversal Street Reconstruction. It builds the scal-

able and robust 3D environmental representations for autonomous driving. Qin et al. [30] employ semantic segmentation to mask transient objects out and learn per-traversal appearance embeddings. 3DGM [20] proposes a self-supervised scene decomposition and mapping framework that leverages repeated traversals and pre-trained vision features to identify static backgrounds. The EUVS benchmark [10] is designed to evaluate view extrapolation quality using multi-traversal data. It also includes a baseline that trains on multi-traversal data confined to a single lane. Existing methods tend to produce blurred synthesized outputs, primarily due to their simplistic modeling of scene dynamics and appearance variations. They also filter out all dynamic objects during reconstruction, while we contend that preserving them is essential for achieving a comprehensive reconstruction and enabling downstream applications.

3. Background

3.1. Preliminary on 3DGS

3D Gaussian Splatting (3DGS), first proposed in [17], effectively reconstructs a scene with a set of 3D Gaussians $\mathcal{G} = \{G_i \mid i = 1, 2, \dots, N\}$, where N is the number of Gaussians. Each $G_i(x)$ is a Gaussian distribution:

$$G_i(x) = \exp \left[-\frac{1}{2}(x - \mathbf{x}_i)^\top \Sigma_i^{-1}(x - \mathbf{x}_i) \right], \quad (1)$$

with learnable properties $\{\mathbf{x}_i, \mathbf{q}_i, \mathbf{s}_i, \alpha_i, \beta_i\}$. Here $\mathbf{x}_i \in \mathbb{R}^3$, $\alpha_i \in \mathbb{R}$ define the position and opacity of the Gaussian. The quaternion $\mathbf{q}_i \in \mathbb{R}^4$ can be converted into a rotation matrix $\mathbf{R} \in \mathbb{R}^{3 \times 3}$, which, along with the scale $\mathbf{s}_i \in \mathbb{R}^3$, determines the covariance matrix Σ_i of the Gaussian, *i.e.*,

$$\Sigma_i = \mathbf{R} \mathbf{S} \mathbf{S}^\top \mathbf{R}^\top, \text{ where } \mathbf{S} = \text{diag}(\mathbf{s}_i). \quad (2)$$

In this way, Σ_i is guaranteed to be positive semi-definite. As for colors, $\beta_i = \{\beta_{i,l,m}\}$ are coefficients for spherical harmonics $\{Y_{l,m}\}_{0 \leq l \leq l_{\max}, 0 \leq m \leq l}$, where each coefficient $\beta_{i,m,l} \in \mathbb{R}^3$ corresponds to RGB channels. Since only $Y_{0,0}$ is rotation-invariant, the coefficient $\beta_{i,0,0}$ defines the natural color of the Gaussian, while other coefficients control view-dependent effects like reflections and shading.

Given a camera pose $\xi = \{\mathbf{W}, \mathbf{K}\}$, including viewing transformation \mathbf{W} from the world coordinates to the camera coordinates and the camera intrinsic \mathbf{K} , a 3D Gaussian can be projected into a 2D one with means and covariance:

$$\mathbf{x}'_i = \mathbf{K} \mathbf{W} \mathbf{x}_i, \quad \Sigma'_i = \mathbf{J} \mathbf{W} \Sigma_i \mathbf{W}^\top \mathbf{J}^\top, \quad (3)$$

where \mathbf{J} is the Jacobian matrix of \mathbf{K} . This 2D Gaussian projection gives the opacity of G_i projected onto the pixel p , denoted as $\alpha_{i \rightarrow p}$, which yields the final opacity by multiplying α_i , the opacity of the Gaussian itself. Combined

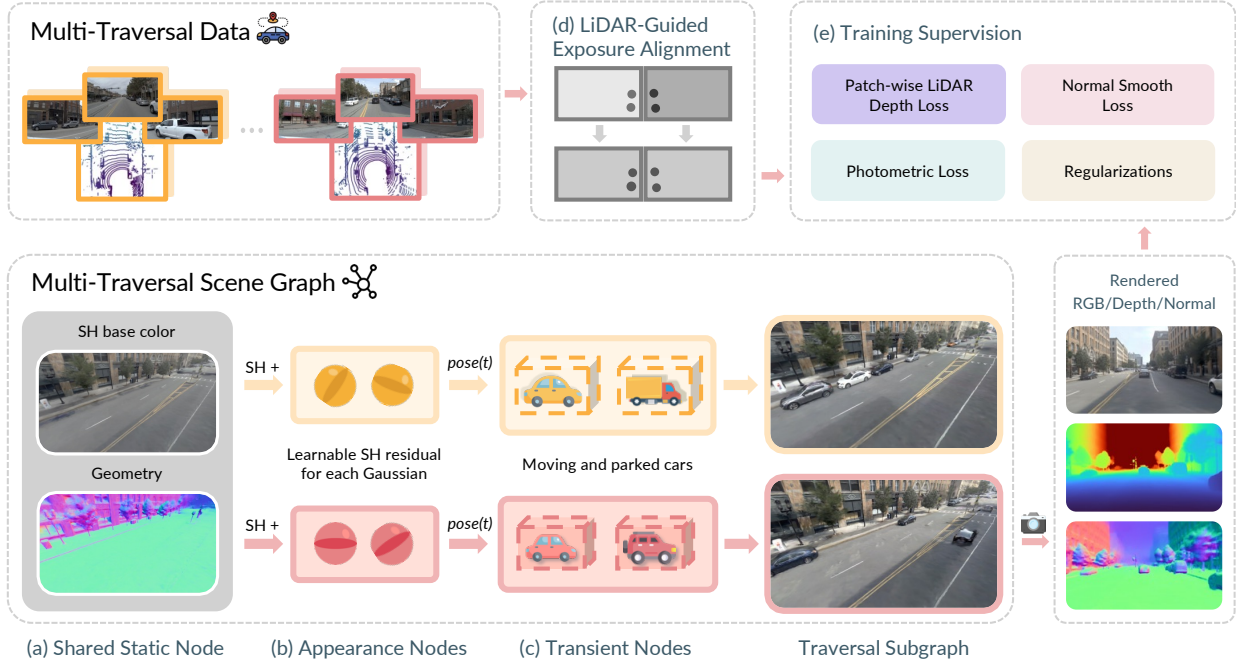


Figure 2. **Overview.** MTGS reconstructs a scene graph from multi-traversal sensor sequences. The scene graph consists of three types of nodes. (a) The rendering of a traversal subgraph starts with a shared static node, representing the time-invariant part of the scene. (b) This is followed by an appearance node that applies traversal-specific appearance effects, such as lighting and shadows. (c) Finally, transient nodes are placed in the background. (d) We align exposure using the overlapping LiDAR point cloud to ensure lighting consistency within the subgraph. (e) Photometric loss and multiple geometric losses are applied to bootstrap the reconstruction fidelity.

with the color $c_{i,p}$ of the Gaussian G_i at pixel p obtained from spherical harmonics, the color at pixel p is determined via volumetric rendering, *i.e.*,

$$c_p = \sum_{i=1}^K c_{i,p} \alpha_{i,p} \prod_{j=1}^{i-1} \alpha_{j,p}, \text{ where } \alpha_{i,p} = \alpha_i \alpha_{i \rightarrow p}. \quad (4)$$

The Gaussians are sorted by their depths from the viewpoint. By comparing the rendered image with the ground truth, we could optimize properties of 3D Gaussians to better the scene reconstruction.

3.2. Problem Formulation

Inputs. The inputs for the task are videos captured in the same block but in different times. In other words, images $\mathcal{I} = \{\mathbf{I}_{t,T} \in \mathbb{R}^{w \times h \times 3} \mid t = 0, \dots, t_T; T = 1, \dots, T_{\text{all}}\}$ are given with corresponding camera poses $\xi_{t,T} = \{\mathbf{W}_{t,T}, \mathbf{K}_{t,T}\}$, where t represents time and T represents traversals. Colored LiDAR point clouds $\mathbf{P}_{t,T} \in \mathbb{R}^{K \times 6}$ are also provided for initialization and sparse depth priors.

Assumptions. We assume that across multiple traversals in the same road block, the background remains largely consistent, *i.e.*, sharing the same geometry despite variations in appearance. Meanwhile, foregrounds, such as moving vehicles and parked cars along the streets, are traversal-variant.

Outputs. The output of the problem is a scene representation f that can render the result $f(\xi, t, T) \in \mathbb{R}^{w \times h \times C}$ captured by camera ξ at time t in traversal T , where $0 \leq t \leq t_T$. C represents the number of expected channels, including RGB, depth, *etc.* Note that the representation should also be able to render results for unseen traversals.

Targets. The target is to optimize f so that its rendered results $f(\xi, t, T)$ are as close as the ground truths of RGB, depth, *etc.*, captured by camera ξ at time t in traversal T .

4. Multi-Traversal Gaussian Splatting

The overall pipeline of Multi-Traversal Gaussian splatting (MTGS) is depicted in Fig. 2. MTGS reconstructs a Multi-Traversal Scene Graph from a set of multi-traversal data, enabling the generation of high-fidelity images. In this section, we first introduce the design of the Multi-Traversal Scene Graph. Next, we describe our approach for tuning appearances across multiple traversals. Finally, we detail the geometric regularization techniques employed in MTGS and training objectives.

4.1. Multi-Traversal Scene Graph

In multi-traversal settings, the state of the scene is determined by time t and traversal T . To model transient objects and appearance changes, we represent the whole scene as

a multi-traversal scene graph built upon 3DGS [17], containing three types of nodes, one shared static node for backgrounds, $\mathcal{G}^{\text{static}}$, multiple appearance nodes for backgrounds, $\mathcal{G}_T^{\text{appr}}$ for traversal T , and multiple transient nodes that exist in exactly one traversal, $\mathcal{G}_{T,k}^{\text{tsnt}}$ for the k -th node in traversal T . The scene in traversal T is thus a subgraph composed of the shared static node $\mathcal{G}^{\text{static}}$, one appearance node $\mathcal{G}_T^{\text{appr}}$ and all transient nodes in the current traversal.

Static Node and Appearance Node. For G_i in the static backgrounds, $\mathcal{G}^{\text{static}}$ provides traversal-invariant and time-invariant properties $\{\mathbf{x}_i, \mathbf{q}_i, \mathbf{s}_i, \alpha_i, \beta_i^{\text{base}}\}$ while the appearance node $\mathcal{G}_T^{\text{appr}}$ provides traversal-wise color residuals in traversal T , $\{\beta_{i,T}^{\text{residual}}\}$. Here, for G_i in traversal T ,

$$\beta_{i,0,0} = \beta_i^{\text{base}}, \text{ and } \{\beta_{i,l,m}\}_{1 \leq l \leq l_{\max}}^{-l \leq m \leq l} = \beta_{i,T}^{\text{residual}}. \quad (5)$$

With such designs, only the coefficient for the rotation-invariant spherical harmonic (SH) $Y_{0,0}$ is shared among different traversals, forcing the Gaussian to learn its natural color and figure out commons in various appearances across traversals to align the geometry of backgrounds. Changes of appearances in different traversals, *e.g.*, lighting, reflections, and overall color tone, are captured by residual coefficients $\beta_{i,T}^{\text{residual}}$, and can then be represented by a linear combination of view-dependent SHs $\{Y_{l,m}\}_{1 \leq l \leq l_{\max}}^{-l \leq m \leq l}$.

In contrast, if some coefficients in $\beta_{i,T}^{\text{residual}}$ are shared, changes caused by various traversals would be mistaken for those caused by various views. When no SH coefficients are shared, the geometry of backgrounds is not aligned, leading to undesired background deviations across traversals.

Transient Node. For Gaussians in $\mathcal{G}_{T,k}^{\text{tsnt}}$, \mathbf{x}_i and \mathbf{q}_i are defined in local coordinates of the node, and can be transformed into world coordinates by

$$\mathbf{x}_i^{\text{world}}(t) = \mathbf{R}_{T,k}(t)\mathbf{x}_i + \mathbf{T}_{T,k}(t), \quad (6)$$

$$\mathbf{q}_i^{\text{world}}(t) = \text{RotToQuat}(\mathbf{R}_{T,k}(t))\mathbf{q}_i, \quad (7)$$

where $\mathbf{R}_{T,k}(t)$ and $\mathbf{T}_{T,k}(t)$ are the rotation matrix and translation of the pose transform of the transient node over time, while $\text{RotToQuat}(\cdot)$ converts a rotation matrix into its corresponding quaternion.

To prevent transient nodes from using floaters to overfit the backgrounds, an out-of-box loss is also introduced as:

$$\mathcal{L}_{\text{oob}} = -\frac{1}{|\mathcal{G}_{T,k}^{\text{oob}}|} \sum_{G_i \in \mathcal{G}_{T,k}^{\text{oob}}} \log(1 - \alpha_i), \quad (8)$$

where $\mathcal{G}_{T,k}^{\text{oob}}$ is the set of Gaussians whose distance from the origin in the local coordinates is larger than $\frac{1}{2}S_{T,k}^{\text{tsnt}} + \theta_{\text{tol}}$. Here, θ_{tol} acts as a tolerance threshold so that the shadow of the foreground is contained in the transient node.

Initialization. We initialize the scene graph structure with automatically labeled 3D bounding bounding boxes from

the dataset [16]. From 3D boxes, we get transient nodes along with their sizes and transformations of poses over time. Gaussian points are initialized from aggregated LiDAR point clouds, with background and transient objects separated. Additionally, we employ point triangulation to initialize far-away Gaussians and randomly sample points on a semisphere to initialize Gaussians representing the sky.

Scene decomposition. We observe that reconstructing transient objects with such subgraph design, rather than simply masking them out, leads to better static reconstruction by preventing the background from overfitting on shadows of transients. Moreover, by this design, all transient objects, not just dynamic ones, can be decomposed from the background and are clearly reconstructed. For example, parked vehicles can be decoupled, as shown in Fig. 2.

4.2. Appearance Modeling

In the multi-traversal setting, appearance modeling is two-fold, the alignment within a traversal and the appearance tuning across multiple traversals. For appearance tuning, we propose appearance nodes in the scene graph to adjust the appearance of backgrounds (See Sec. 4.1). For alignment within traversals, we introduce LiDAR-guided exposure alignment and learnable per-camera affine transforms.

LiDAR-Guided Exposure Alignment. Images might vary in exposure due to various lighting. To align the exposure within images taken by different cameras simultaneously at time t , we project colored LiDAR points at t into these images and adjust the exposure so that pixels corresponding to the same LiDAR point are of the same color.

Learnable Per-Camera Affine Transforms. To enhance consistency between images taken at different time within one traversal, a per-camera affine transform $\text{Aff}(\cdot)$ is attached to refine the color tone, brightness, contrast, and exposure of image $\mathbf{I}_{\text{idx}} \in \mathcal{I}$ by:

$$\text{Aff}(\mathbf{I}) = \mathbf{W}_{\text{idx}}\mathbf{I} + \mathbf{b}_{\text{idx}}. \quad (9)$$

Note that learnable $\mathbf{W}_{\text{idx}} \in \mathbb{R}^{3 \times 3}$ and $\mathbf{b}_{\text{idx}} \in \mathbb{R}^3$ are image-wise, *i.e.*, different parameters for different images.

4.3. Regularization and Training

To achieve high-quality 3D reconstruction and ensure consistency in geometry, we introduce two types of regularization: depth regularization and normal regularization.

Patch-wise LiDAR Depth Loss. The LiDAR depth loss contains an inverse L1 loss and a patch-wise normalized cross-correlation loss. We project sparse LiDAR points into the image plane to obtain sparse LiDAR depth as ground truth. The loss function for this regularization is defined as:

$$\mathcal{L}_{\text{depth}} = \left| \frac{1}{d_{\text{pred}}} - \frac{1}{d_{\text{LiDAR}}} \right|, \quad (10)$$

where d_{pred} is the predicted depth and d_{LiDAR} is the corresponding LiDAR depth.

However, depth from sparse LiDAR points can lead to local overfitting and discontinuity. To address this, we leverage a pre-trained dense depth estimator [29] and enforce a patch-based normalized cross-correlation (NCC) depth regularization [41]. NCC evaluates the similarity between scale-ambiguous pseudo depth and rendered depth patches, ensuring local consistency in depth rendering:

$$\mathcal{L}_{\text{ncc}} = 1 - \frac{1}{|\Omega|} \sum_{p \in \Omega} \sum_{s=1}^{S^2} \frac{\overline{D}_{p,s} D_{p,s}}{\overline{\sigma}_p \sigma_p}, \quad (11)$$

where Ω is the patches set of depth map with size $s \times s$ and stride k . $D_{p,s}$ and σ_p represent a depth patch’s mean-centered values and standard deviations, respectively.

Normal Smooth Loss. To define the normal of a Gaussian, we first note that a Gaussian itself does not inherently possess a normal direction. However, we can derive a geometric normal based on its ellipsoidal shape. Specifically, the normal is defined as the direction of the smallest scaling axis of the Gaussian, which corresponds to its shortest axis in 3D space. Inspired by DN-Splatter [36], for a Gaussian described by a rotation matrix $\mathbf{R} \in \mathbb{R}^{3 \times 3}$ and a scaling vector $\mathbf{s}_i = [s_{i,0}, s_{i,1}, s_{i,2}] \in \mathbb{R}^3$, the normal is computed mathematically as:

$$\hat{\mathbf{n}}_{i,p} = \mathbf{R} \cdot \text{OneHot}(\text{argmin}(s_{i,0}, s_{i,1}, s_{i,2})), \quad (12)$$

where $\text{OneHot}(\cdot) \in \mathbb{R}^3$ returns a unit vector with all zeros except at the position of minimum scaling. To generate per-pixel normal estimates, the corrected normals of 3D Gaussians are first transformed into camera space using the current camera transformation matrix. A per-pixel normal \hat{N} is computed via alpha compositing.

The pseudo normal N is estimated from gradients of the pseudo-depth map, as in 2DGS [13]. To deal with noise in the pseudo normal, we introduce a total variation (TV) loss on the renderer normal. The normal regularization loss is:

$$\mathcal{L}_{\text{normal}} = |\hat{N} - N| + \mathcal{L}_{\text{TV}}(\hat{N}). \quad (13)$$

To obtain a stable Gaussian normal, we add a Gaussian flatten regularization loss to regularize the ratio of the other two axes not exceeding r and minimize the minimum scale axis:

$$\mathcal{L}_{\text{flatten}} = \sum_i \max \left\{ \frac{\max(\mathbf{s}_i)}{\text{median}(\mathbf{s}_i)}, r \right\} - r + \min(\mathbf{s}_i). \quad (14)$$

In the end, all components of MTGS are optimized jointly using the overall training loss:

$$\begin{aligned} \mathcal{L} = & \lambda_r \mathcal{L}_1 + (1 - \lambda_r) \mathcal{L}_{\text{SSIM}} + \lambda_{\text{depth}} \mathcal{L}_{\text{depth}} + \lambda_{\text{ncc}} \mathcal{L}_{\text{ncc}} \\ & + \lambda_{\text{normal}} \mathcal{L}_{\text{normal}} + \lambda_{\text{flatten}} \mathcal{L}_{\text{flatten}} + \lambda_{\text{oob}} \mathcal{L}_{\text{oob}}, \end{aligned} \quad (15)$$

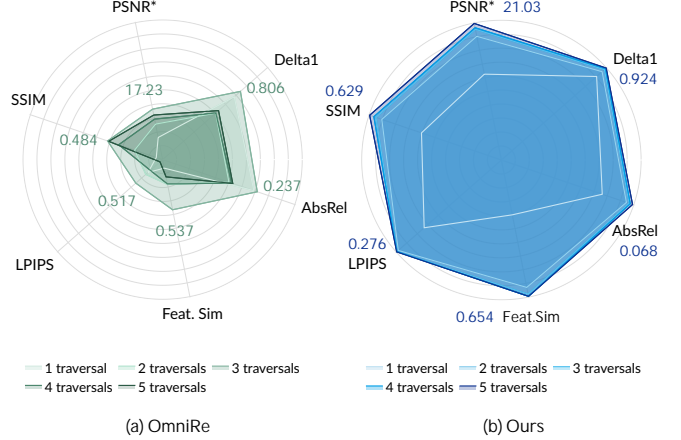


Figure 3. **Novel-view performance when trained with more traversals.** More traversals do not guarantee improvement on existing methods, while our design unleashes their significance. *: affine-aligned PSNR.

where \mathcal{L}_1 and $\mathcal{L}_{\text{SSIM}}$ are photometric losses between ground truth images and renderer images, λ_r , λ_{depth} , λ_{ncc} , λ_{normal} , λ_{flatten} , and λ_{oob} are hyper-parameters.

5. Experiment

5.1. Setup and Protocols

Dataset. The experiments are conducted on dedicated multi-traversal data extracted from nuPlan [16]. This large-scale driving dataset comprises over 100 hours of data, featuring eight surrounding-view images captured at 10 Hz and point clouds merged from 5 LiDAR sensors at 20 Hz. We use all eight views and LiDAR at 10 Hz, with the resolution of 960×540 for images across training and evaluation.

We select six road blocks with multi-traversal data distributed across multiple lanes and evaluate one isolated traversal with minimal spatial overlap with others. During evaluation, non-rigid dynamics are ignored. All transient elements are masked when assessing novel-view traversals, as they are entirely unseen in training.

Implementation Details. Our method is implemented upon open-source repositories, nerfstudio and gsplat [34, 48]. As for unseen traversals, the appearance node of its nearest training traversal is used for appearance tuning. We select three baselines, 3DGS [17], Street Gaussians [45], and OmniRe [3]. The 3DGS baseline is implemented in gsplat, while other baselines are adapted from OmniRe’s codebase. By default, we train all methods with 30k steps using Adam optimizers. For details, please refer to the supplementary.

Metrics. We compute metrics on three aspects. All the metrics are adapted to support calculating with masks.

- **Pixel-level metrics.** We use peak signal-to-noise ratio (PSNR), structural similarity index measure (SSIM) [38], and affine-aligned PSNR [1] for novel-view traversals.

Table 1. **Comparison with SOTA.** ‘ST’ denotes single-traversal reconstruction. ‘MT’ stands for multi-traversal reconstruction. For MT, results on training traversals are averaged and cannot be compared with those in ST directly. The evaluation for novel-view traversal is identical between ST and MT. *: affine-aligned PSNR. †: adapted with multi-traversal transient nodes. **First**, **second**, **third**.

Method		Training Traversal				Novel-View Traversal					
		PSNR \uparrow	SSIM \uparrow	LPIPS \downarrow	AbsRel \downarrow	PSNR* \uparrow	SSIM \uparrow	LPIPS \downarrow	Feat. Sim. \uparrow	AbsRel \downarrow	Delta1 \uparrow
ST	3DGS [17]	25.40	0.775	0.299	0.256	19.15	0.570	0.414	0.514	0.285	0.437
	StreetGS [45]	23.32	0.852	0.304	0.080	17.39	0.473	0.479	0.558	0.157	0.815
	OmniRe [3]	23.64	0.865	0.283	0.081	17.34	0.466	0.474	0.560	0.162	0.805
	Ours	29.43	0.879	0.150	0.094	20.11	0.575	0.313	0.614	0.145	0.879
MT	3DGS [17]	22.04	0.705	0.390	0.332	20.53	0.614	0.388	0.557	0.347	0.312
	StreetGS \dagger [45]	20.57	0.736	0.447	0.097	18.18	0.527	0.488	0.577	0.148	0.826
	OmniRe \dagger [3]	20.91	0.755	0.409	0.092	18.36	0.527	0.460	0.594	0.136	0.859
	Ours	28.04	0.848	0.192	0.094	21.65	0.628	0.265	0.670	0.089	0.904
	Ours (60k)	28.73	0.865	0.169	0.094	21.58	0.620	0.254	0.676	0.091	0.902

Table 2. **Ablation on appearance modeling.** The full model in ID 5 validates the effectiveness of our designs, as well as outperforming existing methods in handling the appearance variations [19]. ‘CamAFF’ refers to per-camera affine, ‘LEA’ denotes LiDAR exposure alignment, and ‘Appr. Node’ represents the appearance node. **First**, **second**, **third**.

ID	Module			Training Traversal				Novel-View Traversal					
	CamAFF	LEA	Appr. Node	PSNR \uparrow	SSIM \uparrow	LPIPS \downarrow	AbsRel \downarrow	PSNR* \uparrow	SSIM \uparrow	LPIPS \downarrow	Feat. Sim. \uparrow	AbsRel \downarrow	Delta1 \uparrow
0				23.46	0.784	0.249	0.105	19.66	0.582	0.308	0.612	0.094	0.901
1	✓			24.95	0.799	0.229	0.090	20.05	0.589	0.293	0.628	0.082	0.912
2	✓	✓		26.16	0.818	0.219	0.086	20.85	0.615	0.281	0.633	0.078	0.914
3	✓		✓	27.08	0.838	0.199	0.087	20.02	0.586	0.288	0.638	0.078	0.914
4		✓	✓	27.59	0.853	0.190	0.084	20.79	0.612	0.274	0.641	0.077	0.914
5	✓	✓	✓	28.51	0.859	0.179	0.085	20.83	0.611	0.271	0.646	0.078	0.914
6	WildGaussians [19]			25.20	0.805	0.229	0.096	19.88	0.577	0.300	0.618	0.087	0.909

- Feature-level metrics. We employ learned perceptual image patch similarity (LPIPS) [51] and DINOv2 [28] feature cosine similarity (Feat. Sim.), which matters more to the downstream visual models [22].
- Geometry-level metrics. We evaluate geometry accuracy with depth-related metrics, including the absolute relative error and $\delta_{1,25}$ (delta 1), between the rendered depth and projected LiDAR depth within an 80-meter range.

5.2. Main Results

We show results in both single-traversal (ST) and multi-traversal (MT) settings in Tab. 1. In ST tests, our method outperforms others in image reconstruction, likely due to its effective inner-traversal appearance modeling. It also achieves the highest quality in novel-view synthesis across all metrics, especially at feature and geometry levels.

In the MT setting, MTGS reconstructs a consistent scene across multiple traversals. Although OmniRe obtains good results on training traversals regarding SSIM and AbsRel, its severe overfitting leads to poor performance on novel-view traversals. In contrast, MTGS consistently delivers the best novel-view synthesis performance. Notably, with additional training iterations (60k), the feature-level metrics further improve, while the geometry metrics tend to converge.

Table 3. **Ablation on modular designs.** Nodes in the scene graph and regularization losses are all crucial for the final performance. ‘tsnt.’ stands for transient. **First**, **second**.

ID	Exp. name	Novel-View Traversal					
		PSNR* \uparrow	SSIM \uparrow	LPIPS \downarrow	Feat. Sim. \uparrow	AbsRel \downarrow	Delta1 \uparrow
0	w/o tsnt. node	20.62	0.607	0.276	0.642	0.086	0.899
1	w/o normal loss	20.82	0.614	0.275	0.643	0.076	0.914
2	w/o depth loss	20.83	0.607	0.264	0.644	0.891	0.613
3	Ours (Full)	20.83	0.611	0.271	0.646	0.078	0.914

A qualitative comparison is shown in Fig. 4. Our baselines produce blurry, artifact-prone images, whereas our method delivers clear, crisp results.

5.3. Ablation Study

Number of traversals. We conduct experiments on three road blocks with six traversals. Traversals in these blocks are not occluded by any buildings or obstructions on-road to ensure that the performance gain of multi-traversal is not simply from seeing the unseen part. As shown in Fig. 3, our method enhances overall rendering quality on novel-view traversals as more traversals are incorporated. In contrast, OmniRe fails to maintain consistent geometry with the increased data. This demonstrates that MTGS effectively



Figure 4. **Visual comparison.** Compared to OmniRE [3] and 3DGS [17], MTGS produces images in higher fidelity, effectively handles appearance variations, and robustly extrapolates to novel views. Notably, our transient node accurately captures moving shadows (red box).

manages the appearance and dynamic variation across multiple traversals, resulting in a more accurate reconstruction of the shared static node. Full results are in the Supplement.

Multi-traversal appearance modeling. In Tab. 2, we demonstrate the effectiveness of our proposed appearance modeling designs by selecting a challenging subset of four road blocks, each containing three training traversals with various appearances. Removing modules from the final design (ID 2-4, compared to ID 5) leads to a performance drop, while incrementally adding modules to the baseline (ID 0-2, and 5) yields significant gains. These findings validate that our strategy effectively captures and reconstructs the diverse appearances across multiple traversals, thereby enhancing both image reconstruction and novel-view synthesis. We also compare our approach with a state-of-the-art Gaussian-based in-the-wild method, WildGaussians [19]. We re-implement its per-camera and per-gaussian appearance embeddings within our pipeline. The results reveal that modeling per-camera appearance in a multi-traversal setting is insufficient, as the limited overlapping regions between cameras complicate the optimization process.

Modular design. We further evaluate additional design choices in MTGS. As shown in Tab. 3, removing the transient node (ID 0) degrades geometry accuracy, likely due to overfitting on the shadows cast by dynamic objects. These results demonstrate that preserving and modeling dynamic information can help multi-traversal reconstruction perfor-

mance. Removing the normal smooth loss (ID 1) adversely affects the feature-level metrics, while removing the depth loss (ID 2) significantly harms learning the geometry.

6. Conclusion and Outlook

In this work, we propose Multi-Traversal Gaussian Splatting (MTGS), the first method capable of reconstructing multi-traversal dynamic scenes with high fidelity. By introducing a novel Multi-Traversal Scene Graph, our approach effectively captures a shared static background while separately modeling dynamic objects and appearance variations across multiple traversals. Extensive evaluations demonstrate that MTGS achieves both high-quality image reconstruction and robust novel-view synthesis, outperforming existing state-of-the-art methods. With its potential to serve as a foundation for photorealistic autonomous driving simulators, MTGS promises to enhance the safety and reliability of autonomous vehicle testing and development.

Limitation and future works. In the current version, non-rigid objects, such as bicycles or pedestrians, are not reconstructed in the scene. However, our method can seamlessly support them by integrating deformable Gaussians or SMPL modeling into the transient node, as demonstrated in [3]. In the shared background, there might be floating artifacts in regions not observed during training traversals, such as the space below parked cars. We also observe that rolling shutter effects, particularly in inverted traversals, introduce

misalignment in the shared geometry. The static geometry of the scene is assumed to remain unchanged. Modeling and reconstruction of unlabeled transient objects and map changes are left for future works. Future endeavors may include simultaneous camera and LiDAR simulation, *e.g.* modeling the appearance diversity of LiDAR intensity and drop rate.

Acknowledgements

We extend our gratitude to Li Chen, Chonghao Sima, and Adam Tonderski for their profound discussions.

References

- [1] Jonathan T Barron, Ben Mildenhall, Dor Verbin, Pratul P Srinivasan, and Peter Hedman. Mip-NeRF 360: Unbounded anti-aliased neural radiance fields. In *CVPR*, 2022. 6
- [2] Li Chen, Penghao Wu, Kashyap Chitta, Bernhard Jaeger, Andreas Geiger, and Hongyang Li. End-to-end autonomous driving: Challenges and frontiers. *IEEE TPAMI*, 2024. 2
- [3] Ziyu Chen, Jiawei Yang, Jiahui Huang, Riccardo de Lutio, Janick Martinez Esturo, Boris Ivanovic, Or Litany, Zan Gojic, Sanja Fidler, Marco Pavone, Li Song, and Yue Wang. OmniRe: Omni urban scene reconstruction. In *ICLR*, 2025. 2, 6, 7, 8, 12
- [4] Bowen Cheng, Ishan Misra, Alexander G. Schwing, Alexander Kirillov, and Rohit Girdhar. Masked-attention mask transformer for universal image segmentation. In *CVPR*, 2022. 12
- [5] Marius Cordts, Mohamed Omran, Sebastian Ramos, Timo Rehfeld, Markus Enzweiler, Rodrigo Benenson, Uwe Franke, Stefan Roth, and Bernt Schiele. The cityscapes dataset for semantic urban scene understanding. In *CVPR*, 2016. 12
- [6] Alexey Dosovitskiy, Lucas Beyer, Alexander Kolesnikov, Dirk Weissenborn, Xiaohua Zhai, Thomas Unterthiner, Mostafa Dehghani, Matthias Minderer, Georg Heigold, Sylvain Gelly, et al. An image is worth 16x16 words: Transformers for image recognition at scale. In *ICLR*, 2021. 12
- [7] Lue Fan, Hao Zhang, Qitai Wang, Hongsheng Li, and Zhaoxiang Zhang. FreeSim: Toward free-viewpoint camera simulation in driving scenes. In *CVPR*, 2025. 3
- [8] Shuo Feng, Haowei Sun, Xintao Yan, Haojie Zhu, Zhengxia Zou, Shengyin Shen, and Henry X Liu. Dense reinforcement learning for safety validation of autonomous vehicles. *Nature*, 2023. 2
- [9] Hao Gao, Shaoyu Chen, Bo Jiang, Bencheng Liao, Yiang Shi, Xiaoyang Guo, Yuechuan Pu, Haoran Yin, Xiangyu Li, Xinbang Zhang, et al. RAD: Training an end-to-end driving policy via large-scale 3dgs-based reinforcement learning. *arXiv preprint arXiv:2502.13144*, 2025. 2
- [10] Xiangyu Han, Zhen Jia, Boyi Li, Yan Wang, Boris Ivanovic, Yurong You, Lingjie Liu, Yue Wang, Marco Pavone, Chen Feng, et al. Extrapolated urban view synthesis benchmark. *arXiv preprint arXiv:2412.05256*, 2024. 2, 3
- [11] Georg Hess, Carl Lindström, Maryam Fatemi, Christoffer Petersson, and Lennart Svensson. SplatAD: Real-time lidar and camera rendering with 3d gaussian splatting for autonomous driving. In *CVPR*, 2025. 2
- [12] Yihan Hu, Jiazhi Yang, Li Chen, Keyu Li, Chonghao Sima, Xizhou Zhu, Siqi Chai, Senyao Du, Tianwei Lin, Wenhai Wang, Lewei Lu, Xiaosong Jia, Qiang Liu, Jifeng Dai, Yu Qiao, and Hongyang Li. Planning-oriented autonomous driving. In *CVPR*, 2023. 2
- [13] Binbin Huang, Zehao Yu, Anpei Chen, Andreas Geiger, and Shenghua Gao. 2D gaussian splatting for geometrically accurate radiance fields. In *SIGGRAPH*, 2024. 6
- [14] Sungwon Hwang, Min-Jung Kim, Taewoong Kang, Jayeon Kang, and Jaegul Choo. VEGS: View extrapolation of urban scenes in 3d gaussian splatting using learned priors. In *ECCV*, 2024. 2, 3
- [15] HyunJun Jung, Nikolas Brasch, Jifei Song, Eduardo Perez-Pellitero, Yiren Zhou, Zhihao Li, Nassir Navab, and Benjamin Busam. Deformable 3d gaussian splatting for animatable human avatars. In *CVPR*, 2023. 2
- [16] Napat Karnchanachari, Dimitris Geromichalos, Kok Seang Tan, Nanxiang Li, Christopher Eriksen, Shakiba Yaghoubi, Noushin Mehdipour, Gianmarco Bernasconi, Whye Kit Fong, Yiluan Guo, et al. Towards learning-based planning: The nuplan benchmark for real-world autonomous driving. In *ICRA*, 2024. 2, 5, 6, 12, 13
- [17] Bernhard Kerbl, Georgios Kopanas, Thomas Leimkühler, and George Drettakis. 3D gaussian splatting for real-time radiance field rendering. *ACM TOG*, 2023. 2, 3, 5, 6, 7, 8, 12
- [18] Mustafa Khan, Hamidreza Fazlali, Dhruv Sharma, Tongtong Cao, Dongfeng Bai, Yuan Ren, and Bingbing Liu. AutoSplat: Constrained gaussian splatting for autonomous driving scene reconstruction. *arXiv preprint arXiv:2407.02598*, 2024. 3
- [19] Jonas Kulhanek, Songyou Peng, Zuzana Kukelova, Marc Pollefeys, and Torsten Sattler. WildGaussians: 3D gaussian splatting in the wild. In *NeurIPS*, 2024. 3, 7, 8
- [20] Yiming Li, Zehong Wang, Yue Wang, Zhiding Yu, Zan Gojic, Marco Pavone, Chen Feng, and Jose M. Alvarez. Memorize what matters: Emergent scene decomposition from multitraverse. In *NeurIPS*, 2024. 3
- [21] Jiaqi Lin, Zhihao Li, Bin Xiao, Huang, Xiao Tang, Jianzhuang Liu, Shiyong Liu, Xiaofei Wu, Fenglong Song, and Wenming Yang. Decoupling appearance variations with 3d consistent features in gaussian splatting. In *AAAI*, 2025. 3
- [22] Carl Lindström, Georg Hess, Adam Lilja, Maryam Fatemi, Lars Hammarstrand, Christoffer Petersson, and Lennart Svensson. Are nerfs ready for autonomous driving? towards closing the real-to-simulation gap. In *CVPR*, 2024. 7
- [23] Ze Liu, Yutong Lin, Yue Cao, Han Hu, Yixuan Wei, Zheng Zhang, Stephen Lin, and Baining Guo. Swin Transformer: Hierarchical vision transformer using shifted windows. In *ICCV*, 2021. 12
- [24] William Ljungbergh, Adam Tonderski, Joakim Johnander, Holger Caesar, Kalle Åström, Michael Felsberg, and Christoffer Petersson. NeuroNCAP: Photorealistic closed-

- loop safety testing for autonomous driving. In *ECCV*, 2024. [2](#)
- [25] Matthew Loper, Naureen Mahmood, Javier Romero, Gerard Pons-Moll, and Michael J. Black. SMPL: a skinned multi-person linear model. *ACM TOG*, 2015. [2](#)
- [26] Ricardo Martin-Brualla, Noha Radwan, Mehdi SM Sajjadi, Jonathan T Barron, Alexey Dosovitskiy, and Daniel Duckworth. NeRF in the Wild: Neural radiance fields for unconstrained photo collections. In *CVPR*, 2021. [3](#)
- [27] Ben Mildenhall, Pratul P Srinivasan, Matthew Tancik, Jonathan T Barron, Ravi Ramamoorthi, and Ren Ng. NeRF: Representing scenes as neural radiance fields for view synthesis. *Communications of the ACM*, 2021. [2](#)
- [28] Maxime Oquab, Timothée Darcet, Théo Moutakanni, Huy Vo, Marc Szafraniec, Vasil Khalidov, Pierre Fernandez, Daniel Haziza, Francisco Massa, Alaaeldin El-Nouby, et al. DINOv2: Learning robust visual features without supervision. *arXiv preprint arXiv:2304.07193*, 2023. [7](#)
- [29] Luigi Piccinelli, Yung-Hsu Yang, Christos Sakaridis, Mattia Segu, Siyuan Li, Luc Van Gool, and Fisher Yu. UniDepth: Universal monocular metric depth estimation. In *CVPR*, 2024. [6](#), [12](#)
- [30] Tong Qin, Changze Li, Haoyang Ye, Shaowei Wan, Minzhen Li, Hongwei Liu, and Ming Yang. Crowd-Sourced NeRF: Collecting data from production vehicles for 3d street view reconstruction. *TITS*, 2024. [2](#), [3](#)
- [31] Johannes Lutz Schönberger and Jan-Michael Frahm. Structure-from-motion revisited. In *CVPR*, 2016. [12](#)
- [32] Johannes Lutz Schönberger, Enliang Zheng, Marc Pollefeys, and Jan-Michael Frahm. Pixelwise view selection for unstructured multi-view stereo. In *ECCV*, 2016. [12](#)
- [33] Matthew Tancik, Vincent Casser, Xinchen Yan, Sabeek Pradhan, Ben Mildenhall, Pratul P Srinivasan, Jonathan T Barron, and Henrik Kretschmar. Block-NeRF: Scalable large scene neural view synthesis. In *CVPR*, 2022. [3](#)
- [34] Matthew Tancik, Ethan Weber, Evonne Ng, Ruilong Li, Brent Yi, Justin Kerr, Terrance Wang, Alexander Kristoffersen, Jake Austin, Kamyar Salahi, Abhik Ahuja, David McAllister, and Angjoo Kanazawa. Nerfstudio: A modular framework for neural radiance field development. In *SIGGRAPH*, 2023. [6](#)
- [35] Adam Tonderski, Carl Lindström, Georg Hess, William Ljungbergh, Lennart Svensson, and Christoffer Petersson. NeuRAD: Neural rendering for autonomous driving. In *CVPR*, 2024. [2](#)
- [36] Matias Turkulainen, Xuqian Ren, Iaroslav Melekhov, Otto Seiskari, Esa Rahtu, and Juho Kannala. DN-Splatter: Depth and normal priors for gaussian splatting and meshing. In *WACV*, 2025. [6](#)
- [37] Ignacio Vizzo, Tiziano Guadagnino, Benedikt Mersch, Louis Wiesmann, Jens Behley, and Cyrill Stachniss. KISS-ICP: In Defense of Point-to-Point ICP – Simple, Accurate, and Robust Registration If Done the Right Way. *RA-L*, 8(2):1029–1036, 2023. [12](#)
- [38] Zhou Wang, Eero P Simoncelli, and Alan C Bovik. Multi-scale structural similarity for image quality assessment. In *ACSSC*, 2003. [6](#)
- [39] Zirui Wu, Tianyu Liu, Liyi Luo, Zhide Zhong, Jianteng Chen, Hongmin Xiao, Chao Hou, Haozhe Lou, Yuantao Chen, Runyi Yang, Yuxin Huang, Xiaoyu Ye, Zike Yan, Yongliang Shi, Yiyi Liao, and Hao Zhao. Mars: An instance-aware, modular and realistic simulator for autonomous driving. *CICAI*, 2023. [2](#)
- [40] Tianyi Xie, Zeshun Zong, Yuxing Qiu, Xuan Li, Yutao Feng, Yin Yang, and Chenfanfu Jiang. Physgaussian: Physics-integrated 3d gaussians for generative dynamics. In *CVPR*, 2024. [12](#)
- [41] Ziyang Xie, Zhizheng Liu, Zhenghao Peng, Wayne Wu, and Bolei Zhou. Vid2Sim: Realistic and interactive simulation from video for urban navigation. In *CVPR*, 2025. [3](#), [6](#)
- [42] Jiacong Xu, Yiqun Mei, and Vishal Patel. Wild-GS: Real-time novel view synthesis from unconstrained photo collections. In *NeurIPS*, 2024. [3](#)
- [43] Jingwei Xu, Yikai Wang, Yiqun Zhao, Yanwei Fu, and Shenghua Gao. 3D streetunveiler with semantic-aware 2dgs. In *ICLR*, 2025. [3](#)
- [44] Chi Yan, Delin Qu, Dan Xu, Bin Zhao, Zhigang Wang, Dong Wang, and Xuelong Li. GS-SLAM: Dense visual slam with 3d gaussian splatting. In *CVPR*, 2024. [12](#)
- [45] Yunzhi Yan, Haotong Lin, Chenxu Zhou, Weijie Wang, Haiyang Sun, Kun Zhan, Xianpeng Lang, Xiaowei Zhou, and Sida Peng. Street Gaussians: Modeling dynamic urban scenes with gaussian splatting. In *ECCV*, 2024. [2](#), [6](#), [7](#), [12](#), [13](#)
- [46] Yunzhi Yan, Zhen Xu, Haotong Lin, Haian Jin, Haoyu Guo, Yida Wang, Kun Zhan, Xianpeng Lang, Hujun Bao, Xiaowei Zhou, et al. StreetCrafter: Street view synthesis with controllable video diffusion models. In *CVPR*, 2025. [3](#)
- [47] Ze Yang, Yun Chen, Jingkang Wang, Sivabalan Manivasagam, Wei-Chiu Ma, Anqi Joyce Yang, and Raquel Urtasun. UniSim: A neural closed-loop sensor simulator. In *CVPR*, 2023. [2](#)
- [48] Vickie Ye, Ruilong Li, Justin Kerr, Matias Turkulainen, Brent Yi, Zhuoyang Pan, Otto Seiskari, Jianbo Ye, Jeffrey Hu, Matthew Tancik, et al. gsplat: An open-source library for gaussian splatting. *JMLR*, 2025. [6](#), [12](#)
- [49] Zhongrui Yu, Haoran Wang, Jinze Yang, Hanzhang Wang, Zeke Xie, Yunfeng Cai, Jiale Cao, Zhong Ji, and Mingming Sun. SGD: Street view synthesis with gaussian splatting and diffusion prior. In *WACV*, 2025. [3](#)
- [50] Dongbin Zhang, Chuming Wang, Weitao Wang, Peihao Li, Minghan Qin, and Haoqian Wang. Gaussian in the Wild: 3D gaussian splatting for unconstrained image collections. In *ECCV*, 2024. [3](#)
- [51] Richard Zhang, Phillip Isola, Alexei A Efros, Eli Shechtman, and Oliver Wang. The unreasonable effectiveness of deep features as a perceptual metric. In *CVPR*, 2018. [7](#)
- [52] Hongyu Zhou, Longzhong Lin, Jiabao Wang, Yichong Lu, Dongfeng Bai, Bingbing Liu, Yue Wang, Andreas Geiger, and Yiyi Liao. Hugsim: A real-time, photo-realistic and closed-loop simulator for autonomous driving. *arXiv preprint arXiv:2412.01718*, 2024. [2](#)
- [53] Hongyu Zhou, Jiahao Shao, Lu Xu, Dongfeng Bai, Weichao Qiu, Bingbing Liu, Yue Wang, Andreas Geiger, and Yiyi

- Liao. HUGS: Holistic urban 3d scene understanding via gaussian splatting. In *CVPR, 2024*. 2
- [54] Xiaoyu Zhou, Zhiwei Lin, Xiaojun Shan, Yongtao Wang, Deqing Sun, and Ming-Hsuan Yang. DrivingGaussian: Composite gaussian splatting for surrounding dynamic autonomous driving scenes. In *CVPR, 2024*. 2

Appendix

A. Implementation Details

We provide key implementation details on datasets, models, and experiments in the supplementary material. To encourage and facilitate further research, we will openly release the whole suite of code and models.

A.1. Dataset

We conduct experiments on customized data from the nuPlan dataset [16]. We use all eight views and LiDAR at 10 Hz, with the resolution of 960×540 for images across training and evaluation.

Handling of inaccurate pose alignment. Since the localization across multiple traversals in nuPlan is imprecise, we employ a LiDAR registration method [37] to align the multi-traversal poses accurately. The camera extrinsic is pre-calibrated but not perfectly synced with LiDAR, causing a pose shift when the car moves. To fix this problem, we composite the motion to the camera extrinsic by interpolation. We further use a camera pose optimizer [44] to handle this misalignment.

Handling of large image distortion. We also note that the camera distortion in nuPlan is severe and could cause bad outputs as in the raw implementation of OmniRe [3]. We undistort the images with OpenCV at optimal mode to preserve the field of view. To alleviate the inaccurate camera intrinsics in nuPlan, we employ several rounds of bundle adjustment of COLMAP [31, 32] to calibrate them.

Use of pre-trained models. The pseudo depth used during training is obtained from UniDepth [29] with a ViT-L [6] backbone. We input the undistorted images and the optimized focal length to UniDepth. Although it generates depth on a metric scale, the depth RMSE is still over 20 meters, which motivates us to apply the NCC loss in our model. To extract semantic masks, Mask2Former [4] with a Swin-L [23] backbone trained on Cityscapes [5] is adopted.

Benchmark. We list the road blocks used in experiments in Tab. 4. The traversals within road blocks are about 100 meters in length. The main comparison is based on all six traversals. The ablation on the number of traversals is based on traversals 0, 1, and 2. The rest of the ablations are based on traversals 0, 1, 2, and 5 with three training traversals. The principle of selecting traversals is shown in Fig. 5.

A.2. MTGS

Transient Node. The initial poses for each transient node are derived from 3D bounding box annotations provided in the nuPlan dataset, which are generated by a pre-trained LiDAR 3D detector and tend to be inaccurate. Therefore, we treat these poses as learnable parameters, following the approach of Street Gaussians and OmniRe [3, 45], without applying a smoothness loss. The poses of static objects are

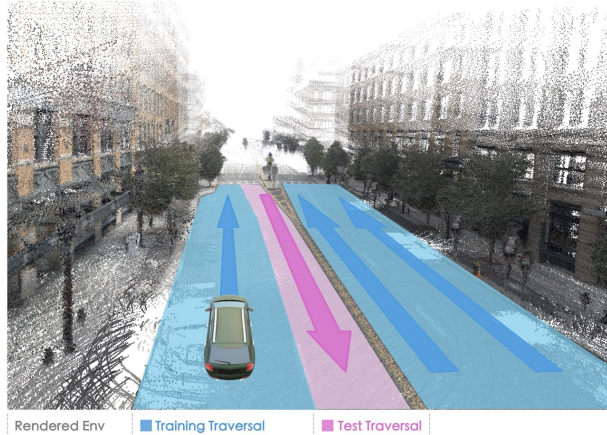


Figure 5. **Illustration of training and test traversals.** We select traversals distributed across multiple lanes and choose the isolated traversal with minimum overlaps.

kept the same across frames. Object with movements of less than 3 meters is considered static.

Optimization. For the optimization process, we employ the Adam optimizer to train our model over 30,000 iterations. All the corresponding hyperparameters are explicitly outlined in Tab. 5. For Gaussian density control, we keep most of the hyperparameters as in the original 3DGS. Since we train the scene on the metric scale without normalization, we adjust the scale threshold of density to 0.2 meters and the scale threshold of culling to 0.5 meters. To remove floaters, we set the gradient threshold of density to 0.001.

Initialization. We initialize a multi-traversal scene graph with metric scale points based on road block-centered coordinates. After aggregating all the LiDAR points, we first remove the statistical outlier to prevent floaters and then perform the voxel downsample with a size of 0.15 meters. We employ point triangulation to initialize far-away Gaussians. For the sky in the scene, we sample 100k points uniformly on a semisphere, with polar angles sampled from $[\frac{\pi}{4}, \frac{\pi}{2}]$ and a radius of two times for the farthest point of the scene.

Losses. Our model is optimized with $\lambda_r = 0.8$, $\lambda_{depth} = 0.5$, $\lambda_{ncc} = 0.1$, $\lambda_{normal} = 0.1$, $\lambda_{flatten} = 1.0$ and $\lambda_{obb} = 1.0$. In the NCC loss, patch size s is set to 32, and k is set to 16. In the Gaussian flatten loss, r is set to 10 and is applied every 10 steps following [40].

A.3. Reproduction of baselines

3DGS [17]. We reproduce 3DGS based on gsplat [48]. We set all the hyperparameters based on the original papers. The scene and the initialized point clouds are normalized with scale factor $5e-3$, which corresponds to 200 meters scene extent.

OmniRe [3]. We adopt its official implementation with default hyperparameters. We perform equivalent data prepro-

Table 4. **Details of selected road blocks.** The city name is from nuPlan [16]. Coordinates are $x_{min}, y_{min}, x_{max}, y_{max}$ in UTM coordinate.

ID	City	Road Block Coordinate	# Traversal
0	us-ma-boston	331220, 4690660, 331190, 4690710	6
1	sg-one-north	365000, 144000, 365100, 144080	3
2	sg-one-north	365530, 143960, 365630, 144060	4
3	us-pa-pittsburgh-hazelwood	587400, 4475700, 587480, 4475800	4
4	us-pa-pittsburgh-hazelwood	587640, 4475600, 587710, 4475660	6
5	us-pa-pittsburgh-hazelwood	587860, 4475510, 587910, 4475570	6

Table 5. **Details of training hyperparameters**

Parameters	Initial LR	Final LR	Warm-up Steps
means	8e-4	8e-6	0
static.features_dc	1.25e-4	1.25e-4	0
appearance.features_rest	1.25e-4	1.25e-4	0
transient.features_dc	2.5e-3	2.5e-3	0
transient.feature_rest	1.25e-4	1.25e-4	0
opacities	5e-2	5e-2	0
scales	5e-3	5e-3	0
quats	1e-3	1e-3	0
camera_pose_opt	1e-4	5e-7	1500
camera_affine	1e-3	1e-4	5000
ins_rotation	1e-5	1e-6	0
ins_translation	5e-4	1e-4	0

cessing steps, including LiDAR registration, bundle adjustment, and distortion correction, which are consistent with our method. Notably, as we do not assess human body reconstruction, we omit the SMPL node component from OmniRe’s pipeline and excluded pedestrians and bicycles during evaluation to ensure fairness.

Street Gaussians [45]. For Street Gaussians, we employ the implementation in the OmniRe repository and the default parameters while maintaining identical data processing protocols.

B. Experiments

Ablation on the extrinsic calibration. As shown in Tab. 6, proper pose alignment significantly boosts both reconstruction and novel-view synthesis performance. Overfitting on inaccurate camera poses degrades view extrapolation. Since our pose alignment process is not fully optimized, improving multi-traversal localization represents a promising direction for enhanced reconstruction.

Reconstruction on big intersections. Fig. 6 shows that MTGS can reconstruction big intersections with occlusions. We exclude such data from our evaluation to ensure that performance gains are not simply due to seeing the unseen regions.

More visualization. As shown in Fig. 7, we show more visualization on extrapolated views of our blocks. The visual-

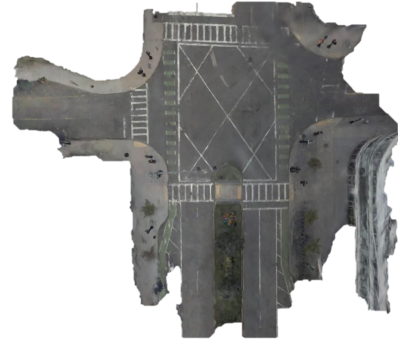


Figure 6. **An intersection with occluded areas.** MTGS can also reconstruct big intersections with occlusions, *e.g.*, buildings and road medians.

ization results of each block are arranged sequentially from left to right according to the temporal order of the traversal. **Ablation on the number of traversals.** Results of all 7 metrics on both training and novel-view traversals are shown in Fig. 8.

Table 6. Ablation on extrinsic calibration.

ID	Module		Training Traversal				Novel-View Traversal					
	LiDAR Registration	CamOptim	PSNR \uparrow	SSIM \uparrow	LPIPS \downarrow	AbsRel \downarrow	PSNR* \uparrow	SSIM \uparrow	LPIPS \downarrow	Feat. Sim. \uparrow	AbsRel \downarrow	Delta1 \uparrow
0			25.45	0.776	0.298	0.131	19.43	0.572	0.374	0.519	0.177	0.700
1	✓		27.70	0.837	0.199	0.082	20.79	0.613	0.281	0.639	0.078	0.914
2	✓	✓	28.51	0.859	0.179	0.085	20.83	0.611	0.271	0.646	0.078	0.914



Figure 7. **More visualization on extrapolated views.** MTGS consistently generates high-quality view extrapolations. However, since all transient nodes are removed when rendering unseen trajectories, floating artifacts appear over car parking areas.

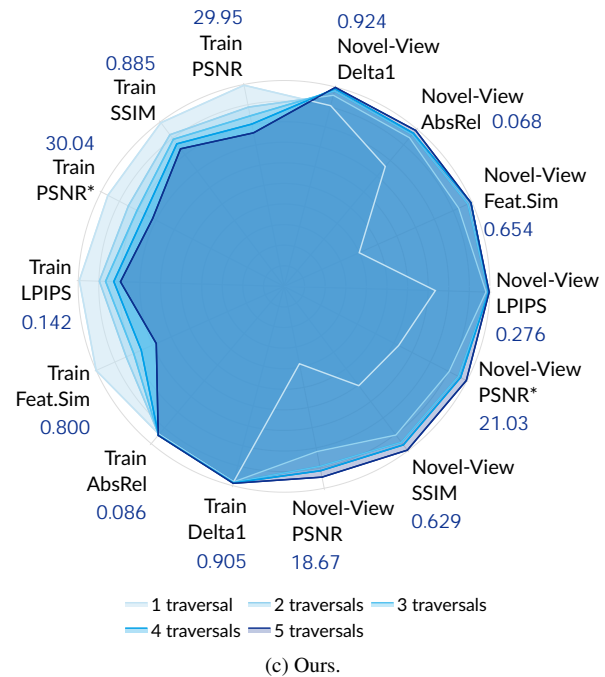
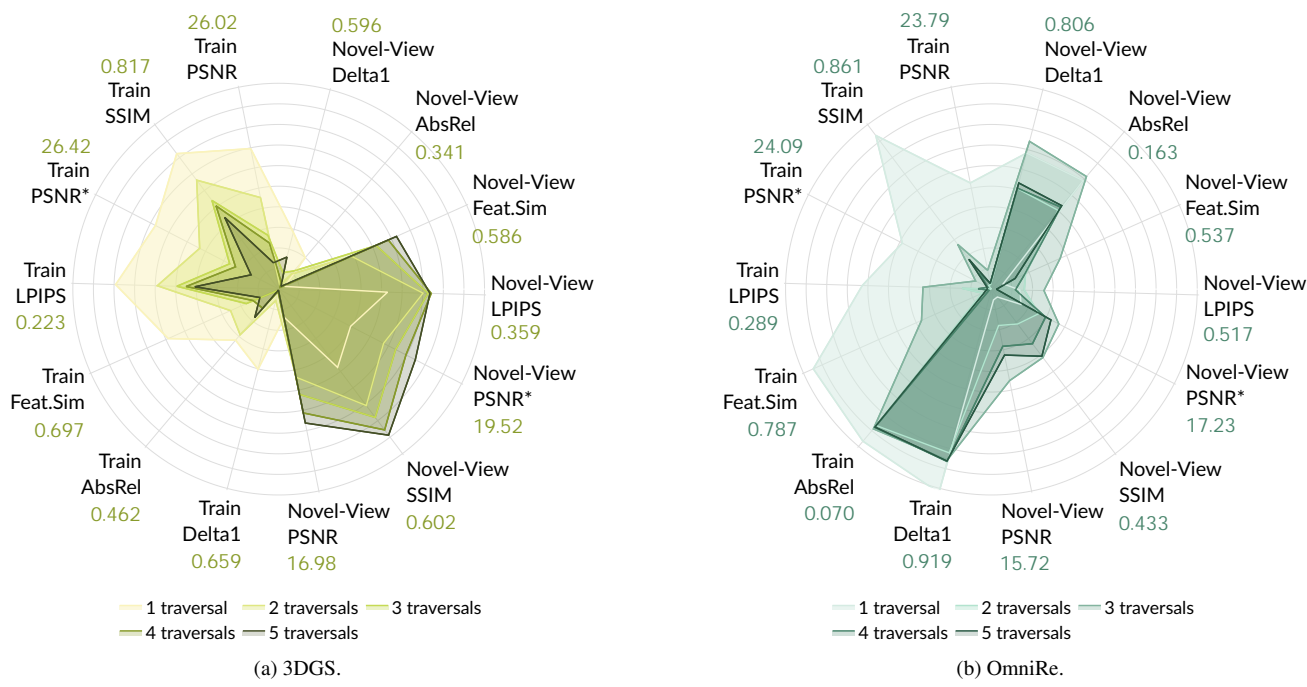


Figure 8. **Performances of three methods when trained on more traversals.** Note that outer rings represent better performance instead of larger scores. More traversals do not guarantee better performances for existing methods while our designs could continually benefit from more traversals used.